Dynamic ray tracing for modeling optical cell manipulation

Ihab Sraj,[1] Alex C. Szatmary,[1] David W. M. Marr,[2,3] and Charles D. Eggleton[1,*]

*[1]Department of Mechanical Engineering, University of Maryland Baltimore County,
Baltimore, Maryland 21250, USA*
*[2]Department of Chemical Engineering, Colorado School of Mines,
Golden, Colorado 80401, USA*
[3]dmarr@mines.edu
[*]eggleton@umbc.edu

Abstract: Current methods for predicting stress distribution on a cell surface due to optical trapping forces are based on a traditional ray optics scheme for fixed geometries. Cells are typically modeled as solid spheres as this facilitates optical force calculation. Under such applied forces however, real and non-rigid cells can deform, so assumptions inherent in traditional ray optics methods begin to break down. In this work, we implement a dynamic ray tracing technique to calculate the stress distribution on a deformable cell induced by optical trapping. Here, cells are modeled as three-dimensional elastic capsules with a discretized surface with associated hydrodynamic forces calculated using the Immersed Boundary Method. We use this approach to simulate the transient deformation of spherical, ellipsoidal and biconcave capsules due to external optical forces induced by a single diode bar optical trap for a range of optical powers.

References and links

1. S. Suresh, J. Spatz, J. P. Mills, A. Micoulet, M. Dao, C. T. Lim, M. Beil, and T. Seufferlein, "Connections between single-cell biomechanics and human disease states: gastrointestinal cancer and malaria," Acta Biomater. **1**(1), 15–30 (2005).
2. G. Y. H. Lee, and C. T. Lim, "Biomechanics approaches to studying human diseases," Trends Biotechnol. **25**(3), 111–118 (2007).
3. J. P. Mills, M. Diez-Silva, D. J. Quinn, M. Dao, M. J. Lang, K. S. Tan, C. T. Lim, G. Milon, P. H. David, O. Mercereau-Puijalon, S. Bonnefoy, and S. Suresh, "Effect of plasmodial RESA protein on deformability of human red blood cells harboring *Plasmodium falciparum*," Proc. Natl. Acad. Sci. U.S.A. **104**(22), 9213–9217 (2007).
4. R. M. Hochmuth, "Micropipette aspiration of living cells," J. Biomech. **33**(1), 15–22 (2000).
5. A. L. Weisenhorn, M. Khorsandi, S. Kasas, V. Gotzos, and H.-J. Butt, "Deformation and height anomaly of soft surfaces studied with an AFM," Nanotechnology **4**(2), 106–113 (1993).
6. P. J. H. Bronkhorst, G. J. Streekstra, J. Grimbergen, E. J. Nijhof, J. J. Sixma, and G. J. Brakenhoff, "A new method to study shape recovery of red blood cells using multiple optical trapping," Biophys. J. **69**(5), 1666–1673 (1995).
7. R. R. Huruta, M. L. Barjas-Castro, S. T. O. Saad, F. F. Costa, A. Fontes, L. C. Barbosa, and C. L. Cesar, "Mechanical properties of stored red blood cells using optical tweezers," Blood **92**(8), 2975–2977 (1998).
8. S. Hénon, G. Lenormand, A. Richert, and F. Gallet, "A new determination of the shear modulus of the human erythrocyte membrane using optical tweezers," Biophys. J. **76**(2), 1145–1151 (1999).
9. A. Ashkin, "Acceleration and trapping of particles by radiation pressure," Phys. Rev. Lett. **24**(4), 156–159 (1970).
10. J. Guck, R. Ananthakrishnan, H. Mahmood, T. J. Moon, C. C. Cunningham, and J. Käs, "The optical stretcher: a novel laser tool to micromanipulate cells," Biophys. J. **81**(2), 767–784 (2001).
11. J. Guck, S. Schinkinger, B. Lincoln, F. Wottawah, S. Ebert, M. Romeyke, D. Lenz, H. M. Erickson, R. Ananthakrishnan, D. Mitchell, J. Käs, S. Ulvick, and C. Bilby, "Optical deformability as an inherent cell marker for testing malignant transformation and metastatic competence," Biophys. J. **88**(5), 3689–3698 (2005).
12. R. W. Applegate, J. Squier, T. Vestad, J. Oakey, and D. W. M. Marr, "Fiber-focused diode bar optical trapping for microfluidic flow manipulation," Appl. Phys. Lett. **92**(1), 013904 (2008).

13. I. Sraj, J. Chichester, E. Hoover, R. Jimenez, J. Squier, C. D. Eggleton, and D. W. M. Marr, "Cell deformation cytometry using diode-bar optical stretchers," J. Biomed. Opt. in press.
14. A. Ashkin, "Forces of a single-beam gradient laser trap on a dielectric sphere in the ray optics regime," Biophys. J. **61**(2), 569–582 (1992).
15. P. B. Bareil, Y. Sheng, and A. Chiou, "Local scattering stress distribution on surface of a spherical cell in optical stretcher," Opt. Express **14**(25), 12503–12509 (2006).
16. G. B. Liao, P. B. Bareil, Y. Sheng, and A. Chiou, "One-dimensional jumping optical tweezers for optical stretching of bi-concave human red blood cells," Opt. Express **16**(3), 1996–2004 (2008).
17. C. Peskin, and D. McQueen, "A three dimensional computational method for blood flow in the heart I. Immersed elastic fibers in a viscous incompressible fluid," J. Comput. Phys. **81**(2), 372–405 (1989).
18. C. D. Eggleton, and A. S. Popel, "Large deformation of red blood cell ghosts in a simple shear flow," Phys. Fluids **10**(8), 1834–1845 (1998).
19. P. Parag, S. Jadhav, C. D. Eggleton, and K. Konstantopoulos, "Roles of cell and microvillus deformation and receptor-ligand binding kinetics in cell rolling," Am. J. Physiol. Heart Circ. Physiol. **295**(4), H1439–H1450 (2008).
20. E. Lac, D. Barthes-Biesel, N. A. Pelekasis, and J. Tsamopoulos, "Spherical capsules in three-dimensional unbounded Stokes flows: Effect of the membrane constitutive law and onset of buckling," J. Fluid Mech. **516**, 303–334 (1999).
21. P. Bagchi, P. C. Johnson, and A. S. Popel, "Computational fluid dynamic simulation of aggregation of deformable cells in a shear flow," J. Biomech. Eng. **127**(7), 1070–1080 (2005).
22. H. C. Van de Hulst, "Light scattering by small particles," John Wiley and Sons, New York. 172–176 (1957).
23. J. Y. Walz, and D. C. Prieve, "Prediction and measurement of the optical trapping forces on a microscopic dielectric sphere," Langmuir **8**(12), 3073–3082 (1992).
24. J. Guck, R. Ananthakrishnan, T. J. Moon, C. C. Cunningham, and J. Käs, "Optical deformability of soft biological dielectrics," Phys. Rev. Lett. **84**(23), 5451–5454 (2000).
25. F. Wottawah, S. Schinkinger, B. Lincoln, R. Ananthakrishnan, M. Romeyke, J. Guck, and J. Käs, "Optical rheology of biological cells," Phys. Rev. Lett. **94**(9), 098103 (2005).
26. M. Lofsted and T. Moller, "An evaluation framework for ray-triangle intersection algorithms," J. Graphics, GPU, Games Tools **10**(2) 13–26 (2005).
27. D. Badouel, "An efficient ray-polygon intersection," in *Graphics Gems*, S. A. Glassner, Ed., (San Diego, CA, USA: Academic Press Professional Inc., (1998), 390–393.
28. T. Moller and B. Trumbore, "Fast, minimum storage ray-triangle intersection," J. Graphics, GPU, Games Tools **2**(1) 21–28 (1997).
29. E. Reinhard, B. E. Smits, and C. Hansen, "Dynamic acceleration structures for interactive ray tracing," Proceedings of the Eurographics workshop on rendering techniques, Brno, Czech Republic, 299–306 (2000).
30. A. Diaz, N. Pelekasis, and D. Barthes-Biesel, "Transient response of a capsule subjected to varying flow conditions: Effect of internal fluid viscosity and membrane elasticity," Phys. Fluids **12**(5), 948–957 (2000).
31. E. Evans, and Y. C. Fung, "Improved measurements of the erythrocyte geometry," Microvasc. Res. **4**(4), 335–347 (1972).

1. Introduction

A change in cellular mechanical properties can be an indication of infection and other pathologies [1,2]; for example, red blood cells (RBC) infected by malaria parasites exhibit significantly different membrane elasticity compared to normal healthy cells. These parasites express proteins that stiffen the RBC membrane by interacting with both the plasma and the cytoskeleton. Suresh and associates [3] have recently shown a difference in the average elastic modulus of normal RBCs and those infected with malaria at different growth stages where, in some cases, the elastic modulus nearly doubled. Such findings suggest that measuring cellular mechanical properties may provide a direct route to either detecting disease at early stages or assessing disease progression at later phases.

Several experimental techniques have been used to measure cellular viscoelastic properties including those relying on direct contact, such as micropipette aspiration [4] and atomic force microscopy [5]. Recently, non-contact methods have also been developed that probe cell mechanical properties using optical trapping [6] through either drag-based deformation [7] or with attached colloids [8]. In this approach, a laser is focused to a diffraction-limited spot with a high numerical-aperture objective, allowing micron-sized objects in solution to be trapped into the region of highest light intensity [9]. With multiple optical traps, biological cells cannot only be manipulated but also deformed, stretched, folded and even rotated. Bronkhorst *et al.* deformed RBCs into a parachute shape using three traps, two at the ends and one in the middle [6]. Henon *et al.* deformed RBCs using two silica beads that were adhered to opposite

sides of the cell surface [8], trapped in dual optical traps, and then pulled by two opposite but equal forces, thereby stretching the cell. This method directs the laser beam on the beads and away from the cell, reducing the risk of thermal damage; however, manipulating beads attached to a cell leads to stress concentration in the membrane that can lead to mechanical injury and/or the measurement of highly localized properties. Addressing these issues, Käs and associates have recently developed an optical stretcher in which they trap individual cells along the axis between two counter-propagating diverging beams thus elongating the cell [10,11]. The use of such opposing bead-free optical stretchers induces smoother and less localized stresses with no focusing required. More recently, Applegate *et al.* [12] implemented optical trapping methods using simplified schemes that take advantage of the nature of micro-fluidic fluid dynamics and use diode laser bars to manipulate particles in micro-scale geometries. This approach employs a single linear optical trap instead of a spot and eliminates the need for expensive associated optics to stretch cells at high-throughput within microfluidic flows [13].

To experimentally quantify an individual cell's elasticity one needs to predict the stress distribution on the cell surface due to the optical trap and measure the induced deformation. To calculate optical forces Ashkin [14] did the first numerical work and determined the total forces of a single-beam gradient laser on solid spheres in the ray-optics (RO) regime. Biological cells, however, are deformable and can change shape under the influence of external flows or applied forces. Because they are directly coupled, the local force distribution and total trapping force can change significantly with the deformation of the cell, and visa versa. To determine the initial stress distribution before cells begin to deform under the influence of induced optical forces Guck *et al.* used the RO method for a dual-beam fiber-optic stretcher and used it to determine the stiffness of RBCs [10,15,16]. The effect of subsequent deformation on the stress distribution was neglected; however, assuming a rigid spherical cell morphology and disregarding deformation in the force calculation is non-physical and may significantly affect cell elasticity predictions.

In this manuscript, we present a numerical method, dynamic ray tracing (DRT) and calculate the cell stress distribution due to light–cell interactions for arbitrary cell shape and simulate the resulting cell deformation in optical traps and stretchers. We do this by combining two numerical methods. The first is a vector-based ray tracer that determines the stress distribution in optical traps on elastic capsules of arbitrary shape and the second employs a fluid-structure hydrodynamic solver to simulate cell deformation due to both external optical forces and cell-fluid interaction. The combined method is used to simulate dynamic cell stretching of different initial shapes, including spheres, oblate spheroids and bi-concave discoids.

2. Numerical method

We implement an advanced RO technique that determines the variable stress distribution on cells in optical traps and uses this to calculate cell transient deformation. DRT takes into account the change in the cell shape due to cell deformability and cell-fluid interaction as opposed to the traditional ray optics method (TRO) that assumes fixed spherical geometries. Cell-fluid interaction is simulated using a hydrodynamic solver based on the immersed boundary method (IBM) which has been used extensively to simulate fluid-structure interaction in biological systems under external flows [17–19]. In this method the fluid governing equations are solved where the viscous stresses are determined and used to find the membrane deformation. Elastic forces are then determined due to the membrane deformability and converted to forces acting on the fluid. These forces are applied to the fluid as body forces. The details of the numerical implementation and validation of the IBM can be found elsewhere [18]. Here, we modify the approach to simulate cell deformation induced by external optical forces found using a ray-tracer that employs the governing physical model

[10] on any discretized cell shape. In our modified IBM code, we incorporate these external optical forces by adding them to the elastic forces and applying them to the fluid.

In the physical model we employ, the cell membrane is assumed to be an infinitesimally thin hyperelastic neo-Hookean material with negligible bending resistance. This model, characterized solely by the membrane stiffness *Eh,* has been commonly used for capsule deformation studies due to its simplicity [18,20,21]. Cells are assumed immersed in an incompressible Newtonian fluid with the same density ρ and viscosity μ as the cytoplasmic fluid but with a different index of refraction. Optical forces on individual elements of the membrane are combined with the membrane elastic forces due to cell deformation into the fluid and added to the source term in the Navier-Stokes equations.

3. Traditional ray optics

Lasers emit rays of light that propagate in straight lines in a medium of constant refractive index until they hit an interface of different index where they change path and speed by refraction and/or reflection. Such a change in light path requires a transfer of the momentum to the interface due to conservation. When the interface is an object, its surface absorbs this momentum and exerts a force proportional to the laser power by Newton's second law. To calculate the optical force distribution, a RO method has been frequently used [10,12,15] where the incoming light is decomposed into individual rays, each with specific intensity and direction, an approach valid when the object is much larger than the wavelength of the light [22]. For spherical objects the condition is given by $2\pi a/\lambda \gg 1$ where a is the radius of the sphere and λ the laser wavelength. For cells of typical radius greater than 3 µm and laser wavelengths less than 1 µm this condition is satisfied [10]. Optical forces are calculated via

$$F_{optical} = \frac{n_m Q P}{c},\tag{1}$$

where n_m is the index of refraction of the buffer medium, c the speed of light in vacuum, P the laser power, and Q is the trapping efficiency, a dimensionless factor representing the amount of momentum transferred. Q is independent of the power applied and depends only on object geometry and the reflectance of the medium. Calculation of Q to date has been for spherical rigid cells [14,23] and shapes [24,25]. In what follows we briefly explain the TRO method and extend this to our implementation of a dynamic ray tracer on cells of arbitrary morphology.

The TRO method makes use of spherical cell symmetry to simplify the trapping efficiency calculation. Q is calculated across the front and back sphere surfaces separately as a function of refractive index and incident laser beam profile, an approach valid because refracted angles can be determined at both front and back interfaces from Snell's law:

$$n_m \sin\alpha = n_p \sin\beta.\tag{2}$$

where α and β and are the incident and refracted ray angles (Fig. 1) and n_m, n_p are the indices of refraction of the two media. Q at any point on the surface can then be expressed as a function of the reflectance R, the original incident angle α, and the refracted angle β. For simplicity Q is typically decomposed into two components (parallel to and perpendicular to the laser axis) as:

$$Q_{front}^{\parallel}(\alpha) = 1 + R(\alpha)\cos(2\alpha) - n(1 - R(\alpha))\cos(\alpha - \beta)$$
$$Q_{front}^{\perp}(\alpha) = R(\alpha)\sin(2\alpha) - n(1 - R(\alpha))\sin(\alpha - \beta)\tag{3}$$

$$Q_{back}^{\parallel}(\alpha) = (1 - R(\alpha))[n\cos(\alpha - \beta) + nR(\beta)\cos(3\beta - \alpha) - (1 - R(\beta))\cos(2\alpha - 2\beta)]$$
$$Q_{back}^{\perp}(\alpha) = (1 - R(\alpha))[-n\sin(\alpha - \beta) + nR(\beta)\sin(3\beta - \alpha) - (1 - R(\beta))\sin(2\alpha - 2\beta)],\tag{4}$$

where $n = n_p / n_m$. In this, the incident light source is considered as an infinite number of rays parallel to the vertical axis, an approximation that works well for large particles. Internal and external reflections within the cell are neglected as their effects rapidly diminish when the reflectance $R<0.005$ for all rays. The magnitude at any point is found via $Q = \sqrt{(Q^\perp)^2 + (Q^\parallel)^2}$ and the total trapping efficiency, and corresponding total force, found through surface integration. It is important to note that these equations for the trapping efficiency Q are valid only on spherical cells and thus, in using TRO, the corresponding optical forces are calculated once initially and kept constant throughout the simulations.
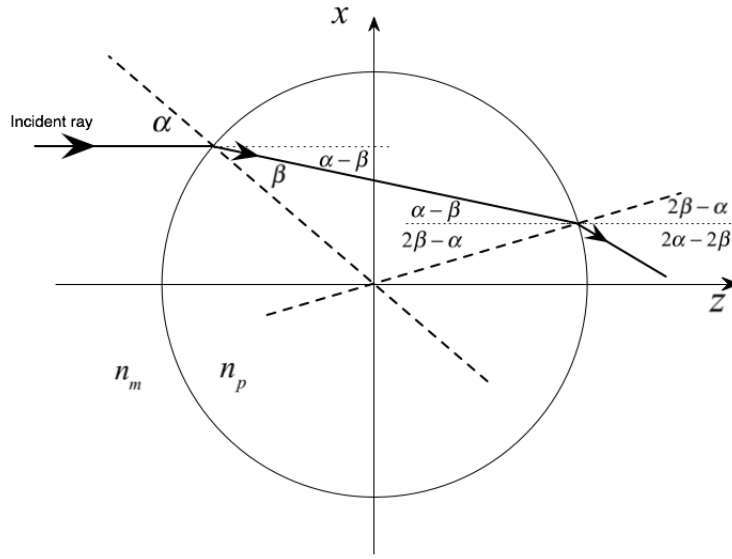
Fig. 1. Angles at the front and back surface of a sphere used in TRO. The angles that incident and refracted rays at the back surface make with the laser axis are α - β and 2α - 2β respectively.

4. Dynamic ray tracing

In simulating the shape evolution of a deformable particle under optical forces, the membrane steady-state geometry is not known *a priori*. Thus, the traditional ray tracing approach is not suitable and another technique is required to calculate the optical forces on evolving complex geometries. We show here how DRT can be used to calculate the optical force distribution on the cell in both its initial stress-free geometry as well as the transient morphologies as the cell deforms in response to combined hydrodynamic and optical forces. In DRT a finite number of rays are issued from a light source with a given intensity and known direction and travel linearly from the source until they intersect with a surface (defined as an interface between two media with different refractive indices). To implement this, we divide the surface into triangular elements with the same surface elements used for both elastic and optical stress calculations. From Eqs. (3) and (4), Q can be determined from incident, refracted and reflected ray angles with the laser axis angle at any point of ray-surface intersection. Thus the elemental optical forces at the first refraction can be expressed as:

$$Q^\parallel = \cos(i) - R(\alpha)\cos(r) - n(1 - R(\alpha))\cos(t)$$
$$Q^\perp = \sin(i) - R(\alpha)\sin(r) - n(1 - R(\alpha))\sin(t),$$

(5)

where i, r and t are the angles formed between the incident, reflected, and transmitted ray with the laser axis (Fig. 2). The angle between the incident ray and the surface normal α remains

the same in the calculation of reflectance *R*. Note here that at any surface *Q* is multiplied by a factor of *1-R* to account for energy loss from previous refractions and thus the general form of *Q* from a medium *x* to another medium *y* can be written as:

$$Q_{x,y}^{\parallel} = (1 - R(\alpha^{'}))[\frac{n_x}{n_m}\cos(i) - \frac{n_x}{n_m}R(\alpha)\cos(r) - \frac{n_y}{n_m}(1 - R(\alpha))\cos(t)],$$

$$Q_{x,y}^{\perp} = (1 - R(\alpha^{'}))[\frac{n_x}{n_m}\sin(i) - \frac{n_x}{n_m}R(\alpha)\sin(r) - \frac{n_y}{n_m}(1 - R(\alpha))\sin(t)],$$

(6)

where α' is the incident angle of the ray in the previous refraction. This general form is useful in DRT where a ray is traced throughout complex shaped cells.

Calculation of the stress distribution therefore requires knowledge of the position where an individual ray hits the surface and the direction of the incoming ray. The first step in implementing a dynamic ray tracer is a ray (semi-line)-triangle intersection algorithm, for which various algorithms techniques are available in the literature [26]. We employ a barycentric approach that determines the intersection of the ray with a plane containing the triangle and then checks whether the point of intersection is inside the triangle [27]. This approach is straightforward and easy to implement but can be computationally consuming; however, optimizing this algorithm does not require much modification [28].

A ray **I** is modeled as a vector with a given origin **e** and direction **d, I = e +** *s***d** where *s* is the distance along the ray measured from the origin in the positive direction (*s > 0*, semi-line). We assume rays are initially parallel to the laser axis, an assumption that works well for non- or weakly-diverging laser diodes (Fig. 2); however, any initial ray direction can be simulated by choosing appropriate ray parameters. We then discretize the surface of the cell into a finite number of non-overlapping 2D triangular elements. In this, each single ray emanating from the source intersects the object at a maximum of one triangle and may not intersect the surface at all. For a triangle with three vertices *A, B* and *C* (Fig. 2), each point on a triangle can be defined using its barycentric coordinates: $P = wA + uB + vC$. For *P* to be inside/on the triangle the sum of the barycentric coordinates must equal one; therefore, *P* can be represented as *P = (1-u-v)A + uB + vC = A + u(B-A) + v(C-A)* with $u > 0, v > 0, u + v < 1$. A given ray **I** then intersects the triangle at *P* when *P = e + s***d** for a given *s*. Combining both conditions we have $P = e + sd = a + u(b - a) + v(c - a)$. For numerical implementation this equation is solved for *s, u* and *v* to find the intersection point and the distance of intersection [26].

Though a ray can hit a 3D shape at multiple locations, we are first interested in the initial contact, as this is the point at which the ray will change direction. To determine all points of intersection, the process is repeated for all triangles to determine a value of *s* for each element. Smaller values of *s* indicate closer objects to the light source; if two objects are both intersected, the one with the smaller value of *s* is recorded as the nearest point of intersection *P*. This procedure can be computationally expensive depending on the number of triangular elements and number of rays. Advanced techniques for saving computational time that avoid calculating ray-triangle intersections over elements in the shadow of elements on the "front-side" of the surface are available in the literature [29].
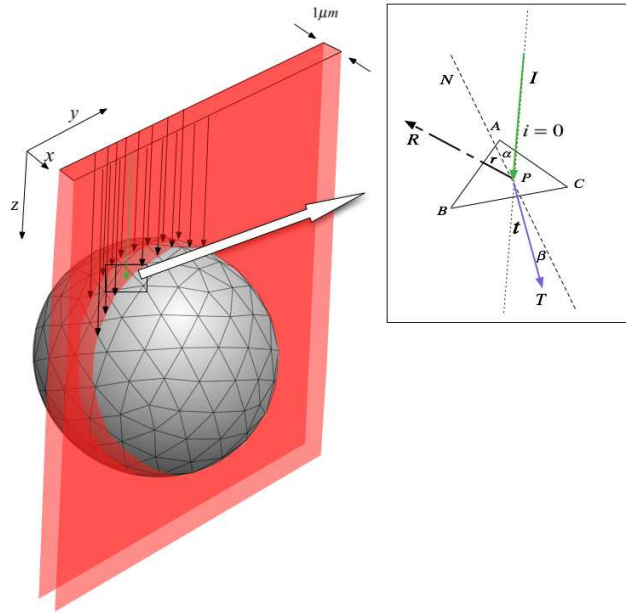
Fig. 2. Dynamic ray-tracing on a spherical cell exposed to a laser sheet from a 1x200 μm long diode bar. The surface of a cell is discretized using a triangular mesh. The inset shows the ray-tracing of a single ray intersecting a triangle of nodes: *A*, *B* and *C* are coordinates of the triangle. *P* is the point of ray-triangle intersection. *N* is the surface normal, *I* the incident ray, *T* the refracted ray and *R* the reflected ray. α and β are the angles of incident and refracted rays with the surface normal; *i, r*, and *t* are the angles with the laser axis *Z*.

Once the point of intersection between an incoming ray and a triangular element is known, one can determine the direction of the reflecting and refracting rays (Fig. 2). Using the normal at a triangle denoted by **N**, the incident angle can be calculated as $\cos\alpha = \mathbf{I} \cdot \mathbf{N} / (|\mathbf{I}||\mathbf{N}|)$. Using Snell's law, Eq. (2), one can then calculate the refracted angle β and the direction vector of both reflected and refracted rays via:

$$\mathbf{R} = \mathbf{I} + (2\cos\alpha)\mathbf{N}$$

$$\mathbf{T} = \frac{n_x}{n_y}\mathbf{I} + \left(-\cos\beta + \frac{n_x}{n_y}\cos\alpha\right)\mathbf{N} \qquad (7)$$

Here, rays change both direction and intensity and continue through the cell until they hit another surface. For refractive index differences typical of cells in water, only refracted rays are traced and reflected rays can be neglected because of their low intensity. A refracted ray is now considered a new ray with a new origin (the current point of intersection *P*) and new intensity. Therefore **I = T** and the previous procedure repeated to find a new contact location. A spherical cell typically has only two intersection locations, one at the front and one at the back surface; however, this approach works for any cell geometry where a ray might encounter multiple external or internal surfaces. For example, in a biconcave capsule, some rays encounter up to four hits at different surfaces. It is important to note that when a ray changes direction it is moving from one medium to another and therefore the indices of refraction are swapped after each hit as the direction of the force changes.

5. Dynamic ray tracer validation

The DRT can be used to find both the initial stress distribution on the cell surface due to light as well as the transient stress distribution upon deforming. Here, we first calculate the initial stress distribution on spherical capsules to validate our method against the TRO method.

5.1 Trapping efficiency calculation

We first calculate the trapping efficiency Q on a sphere using the two methods. The trapping efficiency Q is independent of the light source and is only function of the cell shape and the index of refraction of the cell and the medium n_p = 1.37 and n_m = 1.335 [15]. Here we use Eqs. (3) and (4) for the parallel rays case where Q can be found as a function of the polar angle on both the front and back surface as shown in Fig. 3. The 3D DRT is based on shape discretization and we employ a mesh of 20480 triangles. For comparison, we plot only the calculated Q at the first and second quadrant at a plane parallel to the laser axis passing through the center of the cell representing the front and back surfaces. In these calculations we see an average error of 1.43% across the surface while the maximum error calculated across this plane is 10% at the back surface at the peak value, attributed to the convergence of rays on the back surface. The error on the front surface is relatively small because the gradients in the incoming beam are small and each element is intersected by one ray. Transmitted rays however converge on the backside, causing multiple intersections on some elements and no intersections on other elements, increasing optical force gradients and leading to larger localized error.
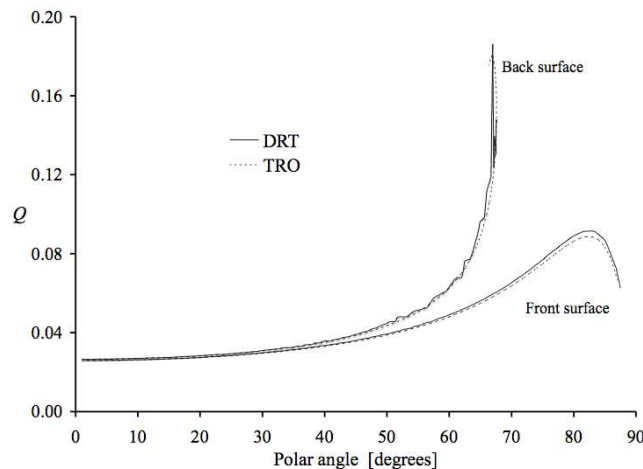

Fig. 3. Trapping efficiency Q on the front and back surface of a spherical cell from both the TRO and DRT.

5.2 Net optical forces

After determining the local Q distribution, one can now calculate induced optical forces by defining the cell size and light source. A spherical cell representing a swollen erythrocyte has a radius a of 3.3 μm. We simulate a linear diode bar light source that is 200 μm long and 1 μm wide [13] (Fig. 2). The laser wavelength is 833 nm leading to $2\pi a/\lambda \approx 25 >> 1$, satisfying the RO condition. Using the TRO for a fixed power of 12 mW/μm, a net force of −7.77 pN on the front surface in the laser axis direction is applied, while 8.23 pN is applied on the back surface, leading to 0.46 pN of net optical force. The magnitude of the induced optical forces compares well with values seen in other work on swollen RBCs [10]. Using the DRT, −7.83 pN is applied on the front surface and 8.50 pN force on the back surface with 0.67 pN of net

optical force, with a calculated error of only 0.75% on the front surface and 3.3% on the back surface.

6. Transient cell deformation

After determining the initial stress distribution, we employ the IBM to deform the cell where the surface optical forces are added as body forces to the surrounding fluid. We then allow the cell to deform until steady state, where the elastic and applied optical forces are equal. Steady-state deformation can then be characterized using the Taylor deformation parameter

$$DF = \frac{L-B}{L+B}, \tag{8}$$

where L and B are the lengths of the major and minor axes of elongated cells in a specified plane. Here we define DF in the x-z plane as the rays are assumed coming parallel to the z axis and the perpendicular component of the optical forces is in the x direction. DF describes the geometrical deformation from perfect spheres ($DF = 0$) to highly elongated morphologies.

Using a membrane stiffness of $Eh = 0.1$ dyn/cm, an unstressed cell is initially placed in a fluid of density $\rho = 1$ g/cm^3 and dynamic viscosity $\mu = 0.8$ cP. The fluid domain is a cube with a side 8x the cell radius a with periodic boundary conditions. The grid used in the simulations has 64^3 nodes with a uniform grid spacing $h = a/8$. The hydrodynamic intrinsic time scale for cell deformation is $t_c = \mu a/Eh$ [30] or $t_c \sim 10^{-3}$ s for our simulation parameters. With this, we use a time step of 10^{-5} s to ensure resolution and numerical stability. In Fig. 4 we show the force at both the front and back surface along with the total net force on the cell function of time. From this we see that both the front and back forces decrease as the cell deforms; however, the net force increases by 6%, using the 12 mW/μm laser power to a constant value when the cell reaches a steady-state shape. In Fig. 5 we show that the net translation force is in the z-direction, pushing the cell away from the light source and deforming the cell as expected for non-converging traps. We note that the initial forces at time $t^* = 0$ are the forces that remain constant using TRO on a sphere.
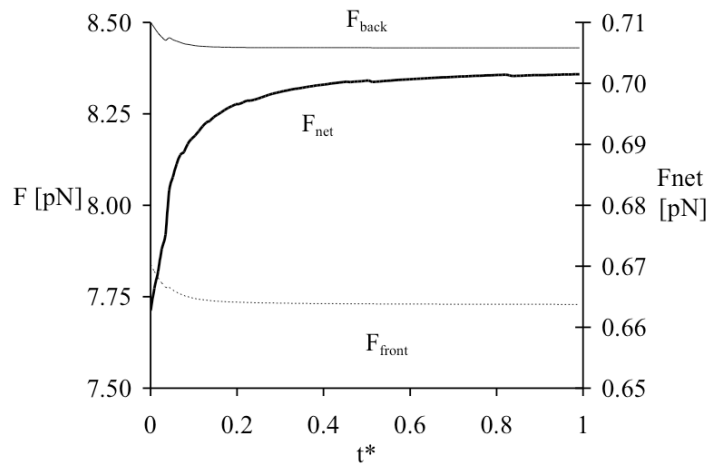

Fig. 4. Transient forces determined using DRT for a laser power of 12 mW/μm. Note, the initial forces at time t* = 0 are the forces that remain constant using TRO on a sphere.
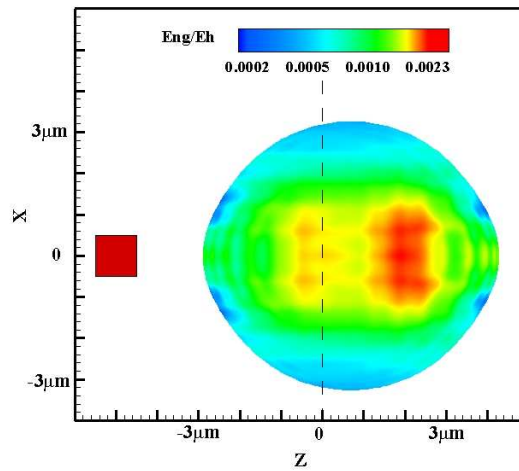
Fig. 5. Side view of the deformed spherical cell when reaching a steady-state shape from a fully 3D simulation colored by the dimensionless elastic energy, *Eng/Eh* (Media 1). The initial radius is 3.3 μm and the diode power is 42 mW/μm. The red square represents the diode bar (not drawn to scale) where the diode long axis is in and out of the figure.

Using higher laser diode powers from 12 mW/μm to 72 mW/μm we simulate the deformation of the cell until it reaches a steady-state shape using TRO and DRT methods. Using TRO we calculate the optical forces initially at the surface of the spherical cell and keep these constant throughout the simulation, thus neglecting the effect of change in shape on the optical force calculation. While using DRT however, the forces are re-calculated every 10 time steps as they vary with the change of the cell shape. We record the net optical force and the corresponding cell deformation when the cell reaches a steady-state shape and plot it for the two methods in Fig. 6. From this we see the non-linear behavior of the net force with laser power as Q changes with cell deformation. Here, calculated values of F_{net} compared to those when neglecting shape change differ by 42% even though the corresponding DF_{xz} changes only 3.65% at the higher laser power. Note that, at lower laser intensities, the two techniques converge as expected.
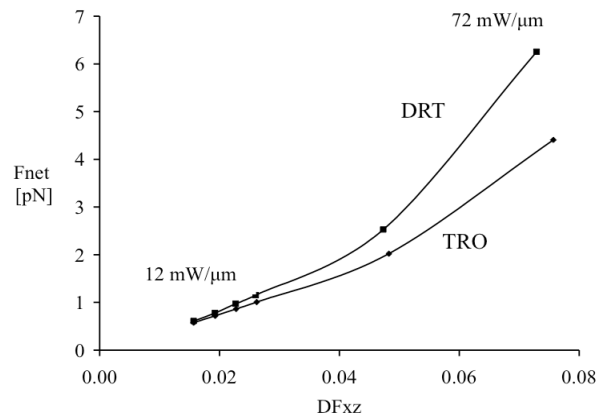

Fig. 6. F_{net} and steady-state deformation as laser power is increased from 12 mW/μm to 72 mW/μm.

7. Non-Spherical Cell Shapes

To test the approach on more complicated structures, we simulate stretching with different initial geometries and laser powers. The complex quiescent biconcave disk shape of normal RBCs prevents the use of TRO as the symmetry along the y-axis allows light rays to hit the RBC surface at four different positions before exiting as illustrated in Fig. 7. To describe the cross section of RBCs, Evans and Fung [31] developed:

$$y = 0.5a[1 - (z/a)^2]^{1/2}[C_0 + C_1(z/a)^2 + C_2(z/a)^4], \quad (9)$$

where $C_0 = 0.207161$, $C_1 = 2.002558$ and $C_2 = -1.122762$, the radius a is 4 μm, and the surface area is 140 μm^2.

In many experimental studies, RBCs are osmotically swollen and assume a spherical shape. To demonstrate the flexibility of DRT, we model both unswollen (biconcave) and swollen (oblate spheroid) RBCs. For the swollen case, we assume an average radius of 2.8 μm, corresponding to a perfect sphere of the same surface area and radius 3.3 μm, and average deformation parameter $DF_{xz} = 0.126$ as seen in experimental work for swollen bovine RBCs [13]. These dimensions lead to a semi major to semi minor axes ratio of 1.28:1.
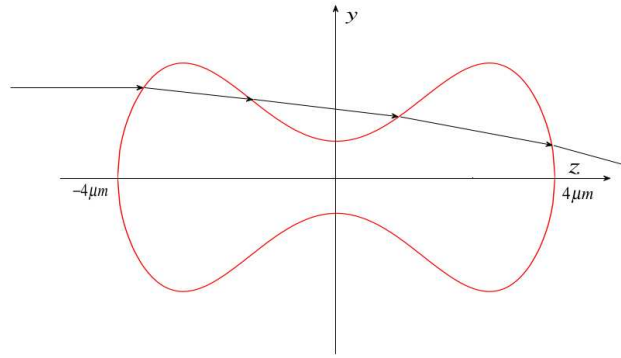

Fig. 7. 2D slice of an RBC with the y-axis as the axis of symmetry. A ray can intersect up to four surfaces.

Using DRT we find the transient stress distribution and simulate swollen and unswollen RBC deformation until steady state. DRT allows us to determine the exact stress distribution on the cell surface without approximation as previously studied [16]. Cells are considered initially static, then exposed to the laser diode bar source, and finally allowed to reach a steady-state shape where DF_{xz} is recorded. Here, the optical forces applied by the diode laser bar are the only external forces on the cell and any flow is induced only by the cell deformability and its translation. Beginning initially with spherical cells for comparison and using a range of laser powers, 12 mW/μm to 72 mW/μm, we see the net optical force induced by a 12 mW/μm laser power is 0.57 pN with a final induced deformation of $DF_{xz} = 0.0158$. Oblate spheroids on the other hand are subjected to more force at identical powers. For example a net force of 0.79 pN is calculated when using the same 12 mW/μm power with a net deformation of $DF_{xz} = 0.0177$, higher than the spherical case (Fig. 8).
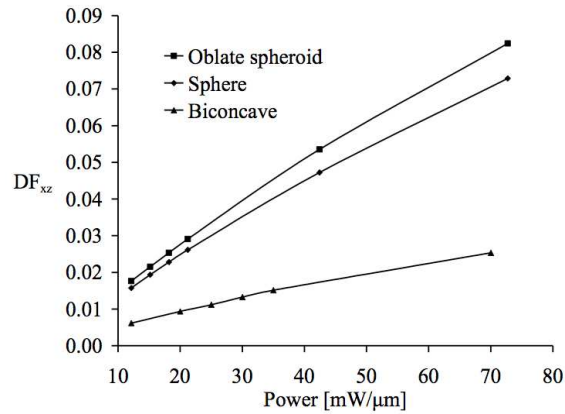
Fig. 8. Comparing deformation at steady state for different RBC shapes.

In this, net deformation was calculated as the final minus the initial deformation (for spheres the initial DF was zero). For the normal RBC case, we observe that the net optical force is significantly higher for the same 12 mW/μm power with a 1.29 pN net optical force induced by rays intersecting the surface at four different positions with stretching forces on both the back and front surface. The net deformation however is smaller $DF_{xz} = 0.0062$. Figures 9(a) and 9(b) (Media 2 and Media 3) shows the steady-state shape of swollen and unswollen RBCs. Table 1 summarizes the net optical forces on different geometries for the same power and corresponding net deformation. From these measurements it is clear that the shape of the cell strongly influences net cell stretching force and deformation.
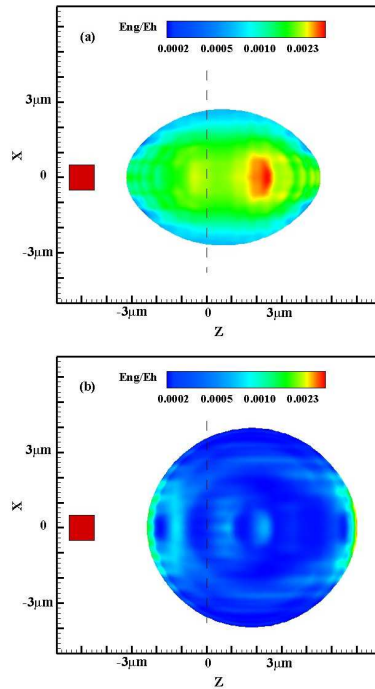
Fig. 9. Side view of the deformed RBC when reaching a steady-state shape from a fully 3-D simulation colored by the dimensionless elastic energy, *Eng*, normalized by *Eh* on (a) oblate sphere of major to minor axis ratio 1.28:1 (Media 2) and (b) biconcave disc of radius 4 μm (Media 3). Diode power is 42 mW/μm.

Table 1. Net optical forces on different RBC shapes of same surface area using 12 mW/μm.

RBC Shape	Sphere	Oblate spheroid	Biconcave discoid
Net optical force	0.57 pN	0.79 pN	1.29 pN
Net deformation	0.0158	0.0177	0.0062

8. Conclusions

We present a dynamic ray tracing method for optical cell manipulation modeling. This method overcomes the limitations of traditional ray optics best suited for light interactions with rigid, spherical cells and allows determination of the transient stress distribution on deformable cells of arbitrary shape subject to cell-fluid interactions. Our simulations indicate that the applied optical forces change substantially with the deformation of the cell, significantly altering prediction of cell forces under conditions of high laser diode powers. We also simulate the deformation of different RBC shapes (spherical, oblate spheroids and bi-concave discoids) to demonstrate the flexibility of the approach for modeling cells of greatly different structure and morphology.

Acknowledgments